Contrib Mineral Petrol (2000) 139: 356–371

Jon Blundy · John Dalton

Experimental comparison of trace element partitioning between clinopyroxene and melt in carbonate and silicate systems, and implications for mantle metasomatism

Received: 15 July 1999 / Accepted: 18 February 2000

Abstract Experiments in the systems diopside-albite (Di-Ab) and diopside-albite-dolomite (Di-Ab-Dmt), doped with a wide range of trace elements, have been used to characterise the difference between clinopyroxene-silicate melt and clinopyroxene-carbonate melt partitioning. Experiments in Di-Ab-Dmt yielded clinopyroxene and olivine in equilibrium with CO_2-saturated dolomitic carbonate melt at 3 GPa, 1375 °C. The experiments in Di-Ab were designed to bracket those conditions (3 GPa, 1640 °C and 0.8 GPa, 1375 °C), and so minimise the contribution of differential temperature and pressure to partitioning. Partition coefficients, determined by SIMS analysis of run products, differ markedly for some elements between Di-Ab and Di-Ab-Dmt systems. Notably, in the carbonate system clinopyroxene-melt partition coefficients for Si, Al, Ga, heavy REE, Ti and Zr are higher by factors of 5 to 200 than in the silicate system. Conversely, partition coefficients for Nb, light REE, alkali metals and alkaline earths show much less fractionation (<3). The observed differences compare quantitatively with experimental data on partitioning between immiscible carbonate and silicate melts, indicating that changes in melt chemistry provide the dominant control on variation in partition coefficients in this case. The importance of melt chemistry in controlling several aspects of element partitioning is discussed in light of the energetics of the partitioning process. The compositions of clinopyroxene and carbonate melt in our experiments closely match those of near-solidus melts and crystals in CMAS-CO_2 at 3 GPa, suggesting that our partition coefficients have direct relevance to melting of carbonated mantle lherzolite. Melts so produced will be characterised by elevated incompatible trace element concentrations, due to the low degrees of melting involved, but marked depletions of Ti and Zr, and fractionated REE patterns. These are common features of natural carbonatites. The different behaviour of trace elements in carbonate and silicate systems will lead to contrasted styles of trace element metasomatism in the mantle.

J. Blundy (✉) · J. Dalton
CETSEI, Department of Earth Sciences,
University of Bristol, Wills Memorial Building,
Bristol, BS8 1RJ, UK
e-mail: Jon.Blundy@bristol.ac.uk

J. Dalton
Department of Geosciences, University of Texas at Dallas,
Richardson, Texas 75083, USA

Editorial responsibility: V. Trommsdorff

Introduction

Carbonate melts are frequently invoked as agents of metasomatic mass transfer in the upper mantle (e.g. Green and Wallace 1988). Such melts can be produced by partial melting of carbonate-bearing mantle rocks at pressure >2 GPa, and temperatures of ≥1000 °C (Wallace and Green 1988; Dalton and Wood 1993). The very low degree of melting involved in carbonatite generation imparts very high incompatible trace element concentrations. Combined with their extreme mobility (Hunter and McKenzie 1989) this makes carbonate melts very efficient metasomatising agents. However, only rarely do metasomatised mantle rocks themselves preserve unambiguous evidence for the passage of a carbonate melt, such as carbonate crystals (e.g. Ionov et al. 1993, 1996; McInnes and Cameron 1994; Schiano et al. 1994; Yaxley et al. 1998). Typically, evidence for the passage of metasomatic carbonate melt in mantle rocks is cryptic, for example the presence of secondary clinopyroxene (cpx) reaction rims on primary orthopyroxene (e.g. Yaxley et al. 1991; Hauri et al. 1993; Coltorti et al. 1998), and/or unusual bulk-rock trace element signatures (e.g. Yaxley et al. 1991; Dautria et al. 1992; Rudnick et al. 1993; Coltorti et al. 1998). In no case is the pristine metasomatic agent itself preserved and its composition must always be inferred through calculation (e.g. Hauri et al. 1993; Rudnick et al. 1993). Such calculations hinge critically on assumptions about

the partitioning of trace elements between mantle minerals (such as cpx) and carbonate melts, for which there are very few experimental data. Consequently, while trace element partitioning between clinopyroxene and silicate melts is increasingly well understood (e.g. Wood and Blundy 1997), there is no consensus on whether partitioning between cpx and carbonate melts is broadly similar in style (Brenan and Watson 1991), or whether it shows significant quantitative differences for some elements (Green et al. 1992; Klemme et al. 1995). If the latter is true, then it may be possible to identify one (or more) chemical "fingerprints" that allow carbonate melt metasomatism to be distinguished from that due to silicate melts or hydrous fluids. The purpose of this experimental study is to quantify the partitioning behaviour of a range of trace cations between cpx and carbonate melts versus silicate melts.

Partitioning of any trace element between cpx and silicate melt is a complex function of pressure (P), temperature (T) and phase composition. It is likely that cpx-carbonate melt partitioning is at least as complex, such that no single set of partition coefficients will suffice under all conditions. Nonetheless, there is a strong temptation to carry out experimental studies on natural systems at mantle pressures and temperatures directly applicable to carbonatite genesis. Unfortunately this approach rarely yields unique results. For example, in the case of mantle melting at the anhydrous lherzolite solidus, two recent studies (Blundy et al. 1998; Salters and Longhi 1999) have produced quite conflicting results, especially for the heavy rare earth elements (REE). Without an understanding of the controls on element partitioning, these conflicts cannot be accounted for, and the geochemist is left unsure which set best describes the mantle melting process. An alternative approach, extensively used in previous work at Bristol University (e.g. Blundy and Wood 1994; Blundy et al. 1995; Law et al. 1998, 2000; Van Westrenen et al. 1999, 2000a; Purton et al. 2000), is to perform experiments on simple systems, with the express intention of isolating and quantifying the individual contributions of ionic radius and charge, P, T and phase composition to the partitioning process. This approach is especially useful in the case of carbonate melt partitioning, where a key objective is to directly compare cpx-carbonate melt partitioning with cpx-silicate melt partitioning. Unless experiments are designed to reduce the number of influential parameters, it is not possible to assess whether any differences in partitioning behaviour are due solely to differences in melt chemistry and structure, or whether they are a consequence of differences in P, T and crystal composition. In this study we report experiments in the simple systems diopside-albite (Di-Ab) and diopside-albite-dolomite (Di-Ab-Dmt) doped with trace elements. We exploit the opportunity to compare cpx-melt partitioning in the presence and absence of carbonate under similar P-T conditions and make a first step in quantifying the distinctive trace element fingerprint of carbonate melts.

Experimental materials and methods

Starting materials were synthesised from trace element doped diopside-albite glasses ($Di_{80}Ab_{20}$), made by glassing diopside and albite gel mixtures. Glass mixes were doped with a suite of trace elements (Li, K, Ga, Rb, Sr, Y, Cs, Ba, La, Sm, Pb) using a 10% nitric acid solution prepared from spectroscopically pure or Analar-grade salts. Ti, Zr, Nb, Nd, Yb, and additional Rb and Ba were added using 1000 $\mu g\ l^{-1}$ AA standard solutions in nitric acid. Approximately 1 g of glass mix was doped with between 450 and 1200 µl of dopant and dried overnight at 100 °C; higher doping levels were employed for glasses used in Di-Ab-Dmt runs (Table 1). The dried mix was denitrified at 350 °C for 30 min and then fused in a covered Pt crucible at 1300 °C for 6 min in order to produce another homogenous glass. For carbonate-bearing (Di-Ab-Dmt) experiments a trace-element-rich $Di_{80}Ab_{20}$ glass was mechanically mixed with variable proportions of a natural Sri Lankan dolomite (B1509) and ground under ethanol for 30 min. (Note that B1509 was not handpicked for purity, and contains tiny silicate and oxide inclusions which, together with the dolomite itself, add to the overall trace element budget of the Di-Ab-Dmt runs, especially for Sr, Zr and K.) Starting materials were then loaded into 1.2 mm o.d. Pt capsules 2 mm in length, dried at 120 °C overnight and welded shut. Capsules for Di-Ab runs were fired at 1000 °C for 1 h prior to welding, to further eliminate adsorbed water. Reconnaissance runs in Di-Ab-Dmt revealed that it was not possible to grow cpx crystals from carbonate melt large enough for SIMS analysis (>15 µm diameter, see below) using reasonable degrees of undercooling. Instead we chose to seed our Di-Ab-Dmt experimental starting mixtures with grains of diopside (Penn State microprobe standard, PXPS 63–1827), ~40 µm in diameter. Compositions of starting materials, including seed, are listed in Table 1.

All partitioning experiments were carried out in 1/2 inch piston-cylinder apparatuses at the University of Texas at Dallas. To minimise vertical thermal gradients across the sample, capsules were run with their long axis horizontally located in the hotspot of talc-Pyrex assemblages with graphite heaters, and alumina spacers and thermocouple sleeves. All parts of the assembly were dried at 120 °C prior to the experiment. The hot piston-out technique was employed without pressure correction for this assembly. Pressures are estimated to be accurate to within ±0.05 GPa of the required pressure. Temperatures were measured with $W_5Re/W_{26}Re$ (Type D) thermocouples, which terminated next to the capsule and are uncorrected for the effect of pressure on thermocouple EMF. Temperatures were controlled to within ±1 °C of the set-point and are estimated to be precise to within ±10 °C. Run times varied from 6 to 30 h in order to assess the time required for the starting materials to reach equilibrium. Proportions of seed, dolomite and $Di_{80}Ab_{20}$ glass in the starting mixes, together with run conditions, duration and results are listed in Table 2.

A second set of experiments (97PC1–3) aimed at synthesising glasses for use as SIMS secondary standards (see below) were carried out at Bristol University. Approximately 50 mg of material was loaded into a 3 mm o.d. Pt capsule and run in a 0.5-inch piston-cylinder apparatus with $BaCO_3$ pressure medium, graphite furnace and Type D thermocouple, using the hot piston-in technique. A −11% friction correction was applied to this assemblage, based upon calibration with PbO-fluxed pyrope-enstatite mixtures (Van Westrenen et al. 1999). Again, no correction was made for any pressure effect on thermocouple EMF. P-T precision is comparable to University of Texas at Dallas experiments. Starting mixes, run details and results are also listed in Table 2. One of this series of runs (97PC2) produced cpx in equilibrium with carbonate melt (Table 2) – phase compositions from this run are also listed in Table 3.

Analytical techniques

At the conclusion of each experiment the capsule was mounted longitudinally in epoxy resin for polishing. Experimental products

Table 1 Major and trace element compositions of starting materials. Major elements (wt%) by EMPA; trace elements (ppm) by SIMS. Average (and 1 s.d.) of *n* analyses. Totals include trace element oxides where analysed. *bd* Below detection. Dashes indicate element not analysed

Element	$Di_{80}Ab_{20}$ glass (97PC3)[a]	$Di_{40}Ab_{10}Dmt_{50}$ glass (97PC1)[b]	Dolomite (B1509)[c]	Diopside seed (XPS 63–1827)
wt%	*n* = 9	*n* = 14	*n* = 16	–
SiO_2	56.65(16)	29.54(16)	–	55.36
Al_2O_3	3.93(5)	2.13(3)	–	bd
FeO	–	–	0.16(5)	0.09
MgO	14.92(9)	18.97(20)	20.5(4)	18.77
CaO	20.48(11)	27.47(25)	32.4(2)	25.70
Na_2O	2.23(7)	1.23(7)	–	0.02
Total	99.24	80.21	53.06	99.94
ppm	*n* = 3	*n* = 3	–	–
Li	673 (3)	560 (65)	–	–
K	236 (3)	224 (19)	–	–
Ti	93.4 (7)	110 (9)	–	60
Ga	16.9 (7)	28.5 (13)	–	–
Rb	352 (7)	337 (36)	–	–
Sr	84 (2)	96 (9)	–	bd
Y	397 (2)	258 (14)	–	–
Zr	85 (1)	61 (2)	–	–
Nb	29 (2)	207 (8)	–	–
Cs	1383 (23)	1380 (135)	–	–
Ba	579 (7)	510 (44)	–	bd
La	1247 (12)	895 (58)	–	–
Nd	150 (1)	107 (9)	–	–
Sm	3103 (45)	2287 (176)	–	–
Yb	95 (1)	64 (3)	–	–
Pb	10 (1)	62 (4)	–	–

[a] $Di_{80}Ab_{20}$ glass starting material used for all Di-Ab runs
[b] Starting material used in some Di-Ab-Dmt runs (e.g. DC6). Other Di-Ab-Dmt runs used different ratios of $Di_{80}Ab_{20}$ glass to dolomite (Table 2). Note that the $Di_{80}Ab_{20}$ glass used to make these starting materials was doped at higher levels than 97PC3
[c] Sri Lankan dolomite. Not handpicked for purity; impurities probably contribute additional K, Sr and Zr to Di-Ab-Dmt starting materials

Table 2 Experimental conditions and results. *Di* diopside; *Ab* albite; *Dmt* dolomite; starting compositions marked by * contained the diopside seed PXPS. *Cpx* Clinopyroxene; *Ol* olivine; *Lc* quenched carbonate liquid; *V* vapour, predominantly CO_2; *Ls(g)* silicate glass; *Ls(q)* silicate quench. Only runs shown in italic were analysed for trace elements

Experiment	Starting composition	Pressure (GPa)	Temperature (°C)	Time (h)	Result
DC1	$Di_{48}Ab_{12}Dmt_{40}$	3.0	1375	12	Cpx, Lc, V
DC2	$Di_{48}Ab_{12}Dmt_{40}$	3.0	1375	24	Cpx, Lc, V
DC6	$Di_{40}Ab_{10}Dmt_{50}$	3.0	1375	12	Cpx, Ol, Lc, V
DC7	$Di_{32}Ab_{8}Dmt_{60}$	3.0	1375	24	Cpx, Ol, Lc, V
DC8	$Di_{48}Ab_{12}Dmt_{40}$*	3.0	1375	6	Cpx, Ol, Lc, V
DC9	$Di_{16}Ab_{4}Dmt_{80}$	3.0	1375	12	Cpx, Ol, Lc, V
DC10	*$Di_{16}Ab_{4}Dmt_{80}$**	*3.0*	*1375*[a]	*24*	*Cpx, Ol, Lc*
DC11	$Di_{16}Ab_{4}Dmt_{80}$*	1.5	1350	24	Fo, Lc, V
DC14	$Di_{16}Ab_{4}Dmt_{80}$*	3.0	1375	6	Cpx, Ol, Lc, V
DC15	*$Di_{16}Ab_{4}Dmt_{80}$**	*3.0*	*1375*	*18*	*Cpx, Ol, Lc, V*
DC16	*$Di_{16}Ab_{4}Dmt_{80}$**	*3.0*	*1375*	*30*	*Cpx, Ol, Lc, V*
DC17	$Di_{80}Ab_{20}$	3.0	1645	6	Cpx, Ls(q), Ls(g)
DC18	$Di_{80}Ab_{20}$	3.0	1665	6	Ls(g)
DC19	$Di_{80}Ab_{20}$	3.0	1655	6	Ls(q), Ls(g)
DC20	$Di_{80}Ab_{20}$	3.0	1625	6	Cpx, Ls(g)
DC22	*$Di_{80}Ab_{20}$*	*3.0*	*1635*	*6*	*Cpx, Ls(q), Ls(g)*
DC23	*$Di_{80}Ab_{20}$*	*0.8*	*1375*	*6*	*Cpx, Ls(g)*
DC26	*$Di_{80}Ab_{20}$*	*3.0*	*1640*	*6*	*Cpx, Ls(q), Ls(g)*
97PC1	*$Di_{40}Ab_{10}Dmt_{50}$*	*3.0*	*1553*	*0.33*	*Lc, V*
97PC2	$Di_{40}Ab_{10}Dmt_{50}$	3.0	1454	1.5	Cpx, Lc
97PC3	*$Di_{80}Ab_{20}$*	*1.8*	*1542*	*6*	*Ls(g)*

[a] True temperature may have been 15 °C higher than this (see text)

containing carbonate melt are difficult to prepare for electron microprobe analysis due to their fragility. Consequently, charges were ground under oil and repeatedly vacuum-impregnated with epoxy resin and re-ground until a satisfactory surface for diamond polishing was obtained. This technique successfully minimises sample degradation and a flat and well-polished surface for electron microprobe analysis (EMPA) can be attained.

Major elements were determined on C-coated mounts by wavelength-dispersive EMPA on a 4-spectrometer JEOL8600 at Bristol University using a 15 kV electron beam. Silicate phases were analysed with a defocused (5–10 μm diameter) 15 nA beam, using the techniques, including counting times, of Blundy et al. (1995). Carbonate melts were analysed using a 5 nA, 20-μm diameter beam calibrated on albite (Na, Al), diopside (Si) and

Table 3 Major element phase compositions. Average (and SD) of *n* EMPA analyses, expressed as wt% oxide. *na* indicates phase not analysed

Run	DC14	DC15	DC16	DC10	97PC2	DC23	DC20	DC22	DC26
P (GPa)	3.0	3.0	3.0	3.0	3.0	0.8	3.0	3.0	3.0
T (°C)	1375	1375	1375	1375	1454	1375	1625	1635	1640
Glass/quench	*n* = 83	*n* = 31	*n* = 27	*n* = 108	*n* = 35	*n* = 16	*n* = 39	*n* = 50	*n* = 19
SiO_2	5.3(6)	4.8(1)	4.9(6)	9.4(14)	23.8(3)	56.7(2)	56.8(3)	56.2(2)	56.6(2)
Al_2O_3	0.55(8)	0.49(9)	0.45(6)	0.91(21)	2.10(5)	5.51(7)	5.35(16)	4.44(8)	4.76(6)
MgO	14.3(6)	14.2(13)	14.2(6)	17.3(13)	18.1(2)	13.0(1)	12.7(5)	14.3(3)	13.95(11)
CaO	38.5(7)	38.3(12)	37.5(7)	34.9(9)	28.6(4)	19.0(7)	18.9(3)	19.9(2)	19.6(1)
Na_2O	0.6(1)	0.54(13)	0.59(8)	0.30(10)	1.41(8)	3.06(7)	3.13(28)	2.37(16)	2.69(7)
Total[a]	59.26[b]	58.59	57.91	63.01	73.96	98.68	96.93	98.41	98.91
Ca/(Ca + Mg)	0.66	0.66	0.65	0.59	0.53	0.51	0.52	0.50	0.50
Olivine	na	*n* = 11	*n* = 6	na	–	–	–	–	–
SiO_2	–	42.9(3)	42.3(4)	–	–	–	–	–	–
Al_2O_3	–	0.12(3)	0.12(2)	–	–	–	–	–	–
MgO	–	57.6(4)	57.3(3)	–	–	–	–	–	–
CaO	–	0.43(5)	0.41(6)	–	–	–	–	–	–
Total[a]	–	101.1	100.1	–	–	–	–	–	–
Cpx	*n* = 14	*n* = 6	*n* = 12	*n* = 13	*n* = 12	*n* = 15	*n* = 16	*n* = 15	*n* = 16
SiO_2	52.0(7)	50.8(6)	50.4(4)	54.4(6)	52.7(7)	56.2(2)	55.8(2)	55.7(2)	55.8(2)
Al_2O_3	6.7(9)	8.5(8)	8.6(3)	3.1(5)	4.7(3)	0.56(12)	1.36(7)	1.14(19)	1.18(14)
MgO	19.2(5)	18.4(4)	18.6(6)	22.2(9)	22.2(8)	20.3(3)	19.43(13)	19.74(16)	19.67(15)
CaO	22.5(5)	22.0(2)	22.1(4)	21.1(5)	19.0(7)	23.5(4)	22.99(15)	22.9(4)	23.10(19)
Na_2O	0.117(16)	0.13(3)	0.13(3)	0.101(12)	0.26(6)	0.179(19)	0.58(3)	0.46(4)	0.49(6)
Total[a]	100.5	99.83	100.87	99.85	98.91	100.3	100.2	99.90	100.09
Cations per 6 oxygens									
Si	1.851	1.819	1.806	1.919	1.888	1.996	1.991	1.992	1.990
Al^{iv}	0.149	0.181	0.194	0.081	0.112	0.004	0.009	0.008	0.010
Al^{vi}	0.131	0.175	0.168	0.047	0.086	0.020	0.048	0.040	0.039
Mg	1.016	0.978	0.992	1.170	1.187	1.072	1.033	1.051	1.046
Ca	0.858	0.845	0.849	0.797	0.730	0.895	0.879	0.876	0.883
Na	0.008	0.009	0.009	0.007	0.018	0.012	0.040	0.032	0.034
Total	4.013	4.007	4.018	4.021	4.022	3.999	4.000	3.999	4.002

[a] Total includes trace elements, where SIMS data are available (Table 4)
[b] Shortfall in carbonate melt analyses approximates wt% dissolved CO_2

dolomite (Ca, Mg). Carbon and oxygen were not analysed. In order to take account of the effect of C on the ZAF correction procedure, we used the "false oxygen stoichiometry" procedure of Lane and Dalton (1994). Some coarser silicate quench mats were analysed by rastering a focused beam over a 15 × 15 μm area. Analytical totals for the carbonate liquids were never 100 ± 1 wt% because of the presence of CO_2. However, the analytical routine used and the H_2O-free nature of the run products (see below) gives us some confidence that the difference from 100% fairly accurately represents the weight fraction of dissolved CO_2.

Trace elements were determined on Au-coated mounts by secondary ion mass spectrometry (SIMS) on a Cameca IMS-4f ion microprobe at the University of Edinburgh, using a 10.69 kV primary beam of O^- ions. Positive secondary ions were accelerated to 4500 V, with an offset of 77–79 V to reduce molecular ion transmission. The energy window was set at ±19 eV. Primary beam currents were in the range 1–15 nA, depending on the spatial resolution required (about 10-μm diameter at 1 nA). The following masses were counted: ^{7}Li, ^{26}Mg, ^{39}K, ^{47}Ti, ^{71}Ga, ^{85}Rb, ^{88}Sr, ^{89}Y, ^{90}Zr, ^{93}Nb, ^{133}Cs, ^{138}Ba, ^{139}La, ^{143}Nd, ^{147}Sm, ^{174}Yb and ^{208}Pb, and normalised to ^{30}Si, as determined by EMPA. FeSi molecular ion interference on Rb was monitored at mass 84; ZrH interference on ^{93}Nb was monitored at mass 95. Both were found to be negligible. Mass 130.5 was measured as background (always < 0.1 counts s^{-1}, and typically zero). NaO interference on ^{39}K was corrected empirically using the EMPA-determined Na content, an Na/NaO ratio of 1290 (R.W. Hinton, personal communication), and an Na^+/Si^+ weight ratio ion yield of 1.075 (Hinton 1990). This amounts to a correction of about 1 ppm K in cpx and olivine, and 5 ppm in matrix. No correction was made for CaAl and CaSi on ^{71}Ga, so these values should be treated with some caution. Count times were adjusted so as to yield a minimum of 100 counts for an analysis of 3–15 cycles. Typical analytical precision is better than ±4% relative for all elements in glass, except Pb (12%); ±10% relative for all elements in cpx, except Nd and Pb (15–20%), Nb and Ba (20–30%) and Cs (±50%, see below); ±1% relative for Li in olivine, ±20–30% for all other elements.

Contamination of crystal analyses by surrounding matrix material is a significant problem when crystal size is only slightly larger than beam diameter (e.g. Beattie 1994). Contamination is most apparent for highly incompatible elements, such as Cs. In this study we used Cs as a monitor of contamination and corrected accordingly the trace element data from crystal analyses with significant glass contamination. This correction rarely amounts to more than a few per cent relative, and is, of course, greatest for Ba and Rb. In the case of Cs itself, we adopted the one or two crystal analyses with the lowest Cs concentration and ascribed to them an arbitrary uncertainty of ±50% relative.

SIMS analyses were calibrated on NIST SRM610 glass for all analyses. Replicate analyses of cpx standards SC8804 (in-house) and KH-1 (Irving and Frey 1984) over a 6-year period demonstrate that calibration on SRM610 yields results for a wide range of trace elements that are accurate to better than ±20% relative (Fig. 1). This is also true of other silicate phases analysed at Edinburgh, including amphibole (Blundy, unpublished data), garnet (Van Westrenen et al. 1999) and orthopyroxene (Blundy, unpublished

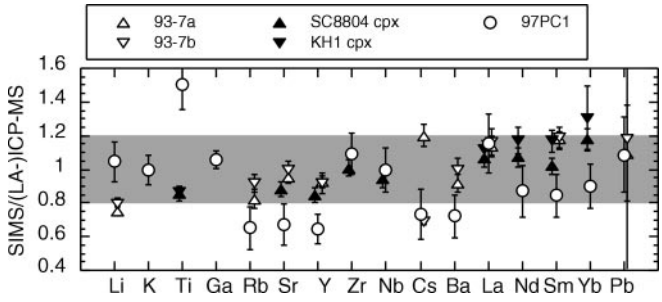

Fig. 1 Comparison of SIMS analyses of mineral and glass standards with laser-ablation and solution ICP-MS analyses of the same materials. 93-7a and 93-7b are $Di_{80}Ab_{20}$ glasses doped with trace elements and analysed by solution ICP-MS. 97PC1 is trace element-doped carbonated glass synthesised from $Di_{40}Ab_{10}Dmt_{50}$ (Tables 1 and 2), and analysed by laser-ablation ICP-MS. SC8804 is a natural San Carlos cpx, analysed by laser-ablation ICP-MS. KH1 is a natural Kilbourne Hole cpx, analysed by INAA (Irving and Frey 1984). *Error bars* are fully propagated 1 s.d. uncertainties based on multiple SIMS analyses over a 6-year period. Note the overall similar trends for all standard materials, indicative of no systematic matrix-dependent bias

data). To ensure SRM610 ion yields were also applicable to Di-Ab glasses, we synthesised two $Di_{80}Ab_{20}$ glasses (93-7a,b) in a vertical quench furnace at 1 atmosphere for analysis both by solution ICP-MS (at Bristol University) and by SIMS. These glasses were doped with a slightly different suite of trace elements to those in our partitioning experiments (i.e. no Zr, Nb, Nd, Yb, and lower Ba). Comparison of ICP–MS and SIMS data indicates that accuracy is again within ±20% relative for all elements (Fig. 1).

Ion yields for carbonate-rich matrices may differ substantially from those for silicate matrices for some elements. It is therefore very important when carrying out ion-microprobe analysis of coexisting phases for partition coefficient determination that any effects due to differences in ion yield be eliminated (or at least evaluated). To do this we synthesised a $Di_{40}Ab_{10}Dmt_{50}$ standard (97PC1), doped with the same trace elements as our other experimental starting materials. Run details are given in Table 2. The quenched run product, which liberated CO_2 gas when the capsule was punctured, was homogeneous carbonated silicate glass (Table 1) containing approximately 20 wt% CO_2, and 0.071(4) wt% H_2O, as determined by FTIR at Bristol University. Of this glass one aliquot was analysed by SIMS as a secondary standard, and a second aliquot was analysed by LA-ICP-MS at VG Elemental Laboratories, Winsford, UK (Fig. 1). For the elements of interest our SIMS analysis of 97PC1 agrees with LA-ICP-MS to within ±25% relative, for all elements except Ti (~45% relative). Significantly the pattern of the SIMS/ICP-MS ratios for this material (Fig. 1) is similar to those of the cpx (SC8804 and KH1) and Di-Ab glass standards (93–7a,b). We conclude that although there are undoubtedly minor differences in secondary ion yields between phases, these are not systematic. Based on the *maximum* difference between silicate and carbonate standards in Fig. 1, we consider our partition coefficients to be accurate to ±20% relative. Demonstrably they are not an artefact of ion-yield differences between crystals and matrix.

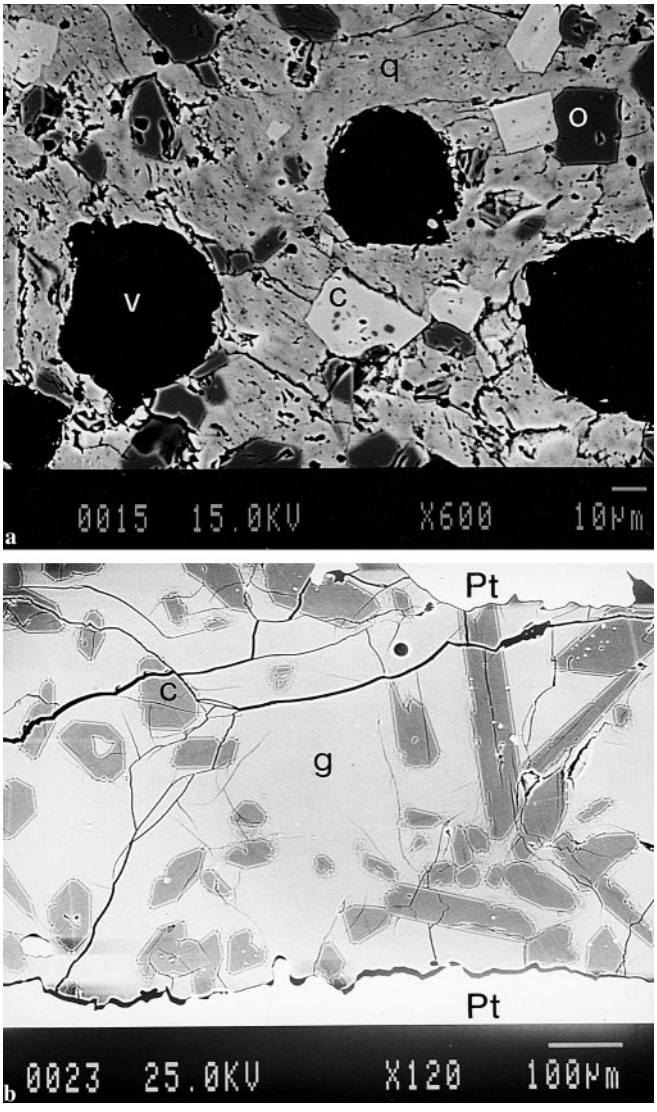

Fig. 2 Back-scattered electron-micrographs of experimental run products. **a** Run DC15 (Table 2) showing euhedral olivine (*o*) and cpx (*c*), some with tiny olivine inclusions, quenched carbonate melt (*q*), and vesicles (*v*), originally filled with CO_2. Note the presence of indistinct light cores to some cpx: these are remains of the diopside seeds. Cpx in this image were not suitable for SIMS analysis: only crystals with regions >15 µm across, lacking seed and olivine inclusions were analysed. *Scale bar* is 10 µm. **b** Run DC23 (Table 2) showing euhedral cpx (*c*) in silicate glass matrix (*g*). Some cpx have glass inclusions, and very thin quench rims. Bright regions at top and bottom of image are Pt capsule. Bright spots in some cpx are also Pt, sequestered from the capsule walls by the melt. *Scale bar* is 100 µm

Experimental results

In Di-Ab-Dmt experiments run products were cpx ± olivine ± vapour and a quenched SiO_2-bearing carbonate melt (Fig. 2a). Quench crystals comprise an intergrowth of carbonate and silicate on a 3–5 µm scale. Equant euhedral cpx + olivine crystals were distributed evenly throughout the charge. The largest cpx were 30–50 µm across, and often showed evidence of a tiny (<15 µm) anhedral diopside seed in the core (Fig. 2a). Some cpx contain tiny rounded olivine inclusions (Fig. 2a). The coexistence of vapour is evinced by the presence of vesicles in many runs (Fig. 2a), and/or the liberation of gas on rupturing the capsule. We conclude that with the exception of DC10 and 97PC2 (Table 2) all Di-Ab-Dmt runs were CO_2-saturated.

The Di-Ab experiments were designed to bracket those of the Di-Ab-Dmt runs in terms of pressure

(3 GPa) and temperature (1375 °C). In these runs the quenched assemblage consisted of euhedral to subhedral cpx (≤300 μm long) in a matrix of feathery quench cpx and clear glass (Fig. 2b). The glass either coalesces at the top of the charge, or occurs as discrete pockets throughout the quench. Crystals tend to accumulate at the base of the charge – only those close to the melt interface were analysed. Some crystals have rounded glass inclusions (Fig. 2b), as observed in other Di-Ab experimental run products (Blundy et al. 1995, fig. 1). The capsule walls show evidence of Pt dissolution in the melt during the run (Fig. 2b). As the solubility of metallic Pt^0 in silicate melts is negligible (≤100 ppb), but increases linearly with fO_2 (Ertel et al. 1999), this observation is suggestive of relatively oxidising conditions during the run.

Phase compositions from Di-Ab and Di-Ab-Dmt runs are listed in Table 3. Analyses of three Di-Ab-Dmt runs of different duration on the same starting material show that crystal and melt compositions for all components, including Al_2O_3 in cpx, become constant after ~15 h (Table 3; Fig. 3), suggesting that this is sufficient time for equilibrium to be achieved. Even after 15 h some unreacted diopside seed can be seen in the cores of large cpx (Fig. 2a); however, overgrown rims were occasionally wide enough for SIMS analysis. In fact, because the starting materials are doped, minor contamination of cpx analyses by natural (i.e. low trace element content) diopside will have little influence on concentration.

Cpx from Di-Ab runs are very similar in composition to those reported by Blundy et al. (1995) under similar conditions. They are characterised by low Al_2O_3 (<1.5 wt%), predominantly occurring as jadeite (Jd) component rather than Ca-Tschermaks (CaTs). The lower pressure run (DC23, 0.8 GPa) has lower Na and Al than the 3 GPa runs, consistent with the pressure sensitivity of Jd partitioning between cpx and silicate melt (Blundy et al. 1995). Coexisting glasses have 4–6 wt% Al_2O_3 and 2–3 wt% Na_2O. Cpx from Di-Ab-Dmt runs DC14–16 have elevated Al_2O_3 (>3 wt%) compared to Di-Ab runs, with CaTs dominating over Jd. Na_2O contents are even lower than those in DC23. These cpx are very similar to those on the CMAS-CO_2 solidus at 3 GPa (Dalton and Presnall 1998a). Coexisting carbonate melts have ~5 wt% SiO_2 and ~0.5 wt% Al_2O_3 contents, again similar to those of near-solidus liquids in CMAS-CO_2 (Dalton and Presnall 1998a) and CMS-CO_2 (Moore and Wood 1998). For example, the molar Ca/(Ca + Mg) ratios of our melts are 0.59–0.66 compared to 0.59 in CMAS-CO_2 at 3 GPa and 1245 °C. The corresponding range in natural dolomitic carbonatites from Cape Verde Islands is 0.53–0.62 (Kogarko 1993). Sweeney (1994) suggests that primary mantle-derived carbonatites have Ca/(Ca + Mg) = 0.50–0.53. The minimum melt composition in the calcite-dolomite system at 2.7 GPa has Ca/(Ca + Mg) = 0.59 (Wyllie and Lee 1998). In contrast the Ca/(Ca + Mg) ratios of melts in other cpx-carbonate partitioning experiments, e.g. 0.78 (Brenan and Watson 1991), 0.75–0.85 (Klemme et al. 1995), are substantially higher. Our experiments are therefore of direct relevance to the petrogenesis of primary dolomitic-carbonatite melts in the mantle, the melt compositions being similar to natural (e.g. Kogarko 1993) and synthetic (Sweeney 1994; Dalton and Presnall 1998a, 1998b; Wyllie and Lee 1998) melts.

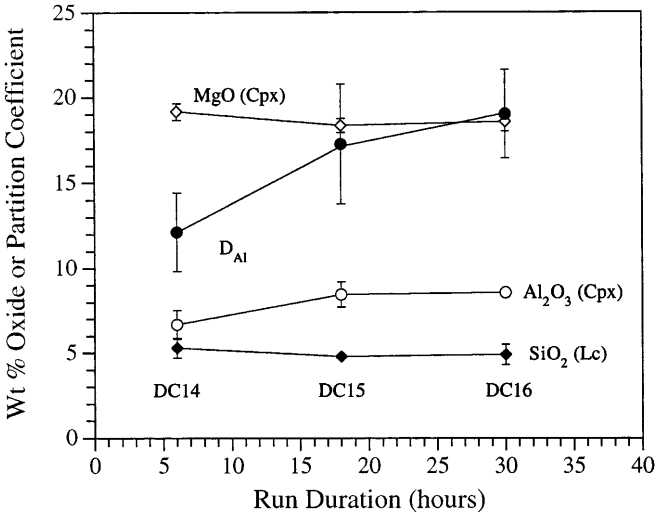

Fig. 3 Effect of run duration on chemistry of Di-Ab-Dmt run products. Selected components only are shown, including slow-diffusing Al_2O_3 in the cpx, and cpx-carbonate melt partition coefficient D_{Al}. *Lc* is carbonate liquid. Note that all compositional parameters converge within 1 s.d. error after around 15 h

Phase compositions in Di-Ab-Dmt run DC10 differ slightly from those in DC14–16, despite all experiments being run under the same nominal conditions (Table 2). Cpx in DC10 has lower Al_2O_3 and higher MgO than in DC14–16, while DC10 melts have higher SiO_2 (~9 wt%), Al_2O_3 (~1 wt%) and slightly lower Ca/(Ca + Mg). Furthermore, DC10 has lower modal olivine and a higher proportion of melt than DC14–16. All of these differences are consistent with DC10 having experienced a slightly higher temperature than DC14–16. Comparison with higher temperature run 93PC2 (Table 3) supports this inference. The exact cause of the proposed discrepancy between thermocouple temperature and run temperature is not known: it may reflect slight changes in sample position relative to the furnace hotspot. In any event the discrepancy need not be large. For example, it is well known that melt SiO_2 content and Ca/Mg ratio increase very rapidly with temperature just above the solidus in CMS-CO_2 (Moore and Wood 1998) and CMAS-CO_2 (Dalton and Presnall 1998b). Consequently, the difference between true and nominal temperature for DC10 may be as little as 15 °C. The absence of vapour vesicles in DC10, in contrast to DC14–16 (Table 2), suggests that the higher melt fraction in this run was able to fully dissolve all CO_2 present in the starting materials.

Olivine has elevated CaO contents (>0.4 wt%) similar to those reported by Brenan and Watson (1991) in

their experiments on olivine-carbonate melt partitioning. In our experiments high CaO is observed even in the largest crystals (50–80 μm diameter), suggesting that this is not an artefact of secondary fluorescence (Dalton and Lane 1996), but a genuine characteristic of olivines in equilibrium with Ca-Mg carbonate melts.

Trace element partitioning

Trace element concentrations in run products and partition coefficients for cpx and olivine are listed in Table 4. Cpx values are plotted in Fig. 4 as ''spidergrams'', ordered according to size and charge, to aid comparison between Di-Ab and Di-Ab-Dmt runs.

Cpx-melt partition coefficients in all runs show a considerable range in magnitude, from $\sim 10^{-4}$ (D_{Cs}) to ~ 20 (D_{Al} and D_{Ga}). Both Di-Ab and Di-Ab-Dmt runs show similar overall patterns (Fig. 4), with an increase in partition coefficient from large to small cations within a given valence group. The anomalous behaviour of Cs in some runs (e.g. DC16) almost certainly reflects small amounts of persistent matrix contamination of the crystal analyses (see above). Such contamination is inevitable when dealing with small crystals and some caution should be used when interpreting D_{Cs}. The anomalous behaviour of Pb has a different origin. Pb^{2+} has slightly larger ionic radius than Sr^{2+} (Shannon 1976) but shows higher partition coefficients than Sr in all runs (Fig. 4). Mixed valence of Pb (i.e Pb^{2+} and Pb^{4+}) is not a plausible explanation for this behaviour, because Pb^{4+} should have a lower partition coefficient than Pb^{2+}. Instead, the behaviour of Pb may reflect analytical problems (note large uncertainties in Fig. 1), or the electronic structure of Pb^{2+} (Blundy and Wood 1994).

Despite the overall similarity in partitioning patterns there are significant differences in cpx-melt partition coefficients between Di-Ab and Di-Ab-Dmt runs. Di-Ab-Dmt runs are characterised by much higher D values for some highly charged cations (e.g. Zr, Ti, but *not* Nb) and network-forming cations (Ga, Al, Si). For REE Di-Ab-Dmt runs show a greater increase from D_{La} to D_{Yb} than do Di-Ab runs (Fig. 4). Partition coefficients for 1+ and 2+ cations are very similar. Possible causes of these differences are discussed below.

There are lesser differences in partition coefficients between different runs on Di-Ab and Di-Ab-Dmt experiments. In the case of Di-Ab the lower pressure run DC23 (0.8 GPa) shows lower partition coefficients for alkali elements than those at 3 GPa counterparts, in keeping with their pressure-sensitive nature (Blundy et al. 1995). For the Di-Ab-Dmt runs, experiment DC10 has lower partition coefficients for the more highly charged cations than DC15 and DC16. For most elements the partition coefficients from DC10 are intermediate between those of DC15–16 and those of the Di-Ab runs. This may be due to either the higher SiO_2 content of the melt in DC10, the lower CaTs content of the cpx, or its higher putative run temperature.

Olivine-melt trace element partition coefficients from Di-Ab-Dmt runs (Table 4) are considerably lower than those for cpx for all elements except Li, for which $D^{ol\text{-}melt}$ is approximately 30% higher, as noted by Brenan et al. (1998) in basaltic liquid. REE partition coefficients increase rapidly with atomic number, as is well known from silicate melt partitioning studies (e.g. Beattie 1994). D_{Yb} is comparable to that observed in the olivine-carbonate melt partitioning study of Brenan and Watson (1991) at 1.5 GPa and 1150 °C (i.e. 0.06–0.12), and in several olivine-basalt partitioning studies (e.g. Colson et al. 1988; Beattie et al. 1991). Olivine-melt partitioning of Ca is almost identical to that observed by Brenan and Watson (1991) for carbonate melts, but is approximately three times lower than observed in basalt melt partitioning studies, even after allowing for temperature and elevated D_{Mg} in the carbonate melt runs (Watson 1979; Beattie et al. 1991). Conversely, D_{Al} is more than 10 times larger than values determined in basaltic systems at 3 GPa and 1600–1800 °C (Taura et al. 1998), and 40 times larger than at atmospheric pressure (Colson et al. 1988).

Compositional effects

There are clear differences between cpx-melt partitioning in the Di-Ab and Di-Ab-Dmt runs. We can directly compare trace element partitioning in these two systems by normalising the silicate melt partition coefficients to the carbonate melt partition coefficients to give $D_{cpx\text{-}sil}/D_{cpx\text{-}carb}$ on an isothermal or an isobaric basis (Fig. 5a). As the design of our experiments serves to minimise the effects of P and T, the cause of the variations in Fig. 5a must be compositional in origin. There are two possibilities: differences in melt chemistry or differences in crystal chemistry.

In the case of crystal chemistry, it is well known that partition coefficients for many elements increase with cpx CaTs content (e.g. Gaetani and Grove 1995; Lundstrom et al. 1998; Hill et al. 2000). This is consistent with our observation of elevated partition coefficients in Di-Ab-Dmt runs, which have high CaTs ($\sim$16 mol%) compared to Di-Ab runs ($\sim$1 mol%; Table 3). The effect of CaTs is greatest for highly charged cations entering the small M1 site in cpx, such as Ti and Nb (Hill et al. 2000). In Fig. 5b we also plot the ratio of partition coefficients for low and high CaTs cpx using the 0.1 MPa isothermal data of Lundstrom et al. (1998), at 1275 °C, and Hill et al. (2000), 1218 °C, which show a range in CaTs contents of 1–6 and 14–28 mol% respectively. The overall pattern is similar to $D_{cpx\text{-}sil}/D_{cpx\text{-}carb}$; however, the fractionation is not as extreme, and in some cases shows the opposite sense to what we observe. For example, the 0.1 MPa CMAS experiments of Gaetani and Grove (1995) show that D_{Ce} is more

Table 4 Trace element compositions of run products and partition coefficients. Carbonate melt experiments shown in italic; others are silicate melt. *n* Number of analyses. All trace elements (in ppm) determined by SIMS. A dash denotes below detection.1 SD uncertainty quoted in terms of last significant digits. Nernst partition coefficients for trace elements (this table) and major elements (Table 3). 1 SD uncertainty by normal error propagation

Run	*DC15*			*DC16*			*DC10*		DC23		DC26		DC22	
Phase (*n*)	Cpx (4)	Olivine (3)	Glass (3)	Cpx (2)	Olivine (1)	Glass (4)	Cpx (3)	Glass (7)	Cpx (4)	Glass (5)	Cpx (4)	Glass (3)	Cpx (2)	Quench (2)
ppm														
Li	18(3)	24(2)	189(8)	17.1(5)	24.3(3)	190(13)	17.2(6)	86(13)	44(5)	1016(63)	73(9)	898(13)	72.2(2)	977(84)
K	4.3(18)	–	183(34)	13(4)	–	163(18)	9(4)	154(49)	1.5(4)	388(35)	4.5(19)	402(4)	40.6(5)	385(26)
Ti	37(6)	1.1(2)	42(3)	44(4)	1.06(16)	52(2)	14.5(15)	34(2)	23(5)	110(2)	18.4(7)	101(1)	16.8(6)	91.6(15)
Ga	13(7)	0.74(9)	1.0(3)	25(1)	–	1.28(15)	4.3(19)	1.6(2)	6.9(20)	16.9(5)	3.1(8)	16.8(1)	4.12(4)	19.7(3)
Rb	0.7(4)	–	114(15)	1.1(3)	–	117(10)	0.51(10)	93(31)	0.23(5)	536(60)	0.27(6)	506(10)	0.7(2)	350(19)
Sr	4.7(1)	–	57(7)	4.0(4)	–	57(3)	3.7(2)	47(4)	15.2(14)	120(6)	22(1)	107(1)	22(1)	113(1)
Y	45(12)	0.24(7)	42(4)	50(7)	–	47(3)	22(1)	43(4)	113(12)	498(8)	82(4)	460(5)	82(1)	433(8)
Zr	57(20)	0.22(14)	71(2)	200(100)	0.08(2)	140(8)	19(3)	130(9)	11(4)	193(7)	2.3(1)	96(1)	2.9(4)	102(2)
Nb	0.9(4)	–	58(4)	0.8(3)	–	60(3)	0.8(5)	47(8)	0.9(6)	45(6)	0.11(2)	29.6(5)	0.11(3)	23.6(4)
Cs	0.04	–	415(46)	2.2(4)	–	416(34)	0.52(10)	295(120)	0.18(11)	1789(158)	0.4(3)	1649(33)	0.19(5)	1335(85)
Ba	0.03(1)	–	147(10)	0.8(1)	–	156(10)	0.71(17)	113(20)	0.6(3)	905(53)	1.4(1)	812(9)	2.2(3)	796(21)
La	9.3(13)	–	181(19)	13(1)	–	196(11)	6.0(7)	145(17)	103(19)	1732(44)	72(9)	1550(8)	82(4)	1485(25)
Nd	5.1(6)	–	22(3)	9(4)	–	23(2)	3.0(3)	19(2)	31(5)	193(5)	20.7(9)	179(2)	22.5(1)	172(5)
Sm	179(30)	0.20(4)	496(47)	222(28)	–	513(30)	106(11)	411(40)	826(103)	4008(60)	516(94)	3753(5)	602(2)	3500(100)
Yb	10(4)	0.32(17)	10.6(9)	15(3)	0.60(8)	11.9(8)	6.3(7)	10.6(9)	26(3)	116(3)	19(1)	108(1)	19.6(4)	105(3)
Pb	8(5)	4.50(8)	11(1)	13(3)	5.7(7)	8.3(6)	3.1(2)	6.4(9)	7(3)	8.3(5)	4(3)	9.5(3)	6.4(8)	37(12)
Partition coefficients														
Si	10.6(3)	8.93(20)	–	10.3(13)	8.6(11)	–	5.8(9)	–	0.991(5)	–	0.986(4)	–	0.992(5)	–
Al	17(3)	0.24(8)	–	19(3)	0.27(6)	–	3.4(10)	–	0.10(2)	–	0.25(3)	–	0.26(4)	–
Mg	1.29(12)	4.1(4)	–	1.31(7)	4.04(17)	–	1.29(11)	–	1.56(2)	–	1.41(2)	–	1.39(3)	–
Ca	0.575(19)	0.0112(14)	–	0.589(15)	0.0109(16)	–	0.60(2)	–	1.24(2)	–	1.176(12)	–	1.15(2)	–
Na	0.24(8)	–	–	0.22(6)	–	–	0.34(12)	–	0.058(6)	–	0.184(22)	–	0.20(2)	–
Li	0.095(16)	0.127(12)	–	0.090(7)	0.126(9)	–	0.20(3)	–	0.043(6)	–	0.081(10)	–	0.074(6)	–
K	0.024(11)	–	–	0.08(3)	–	–	0.06(3)	–	0.0039(11)	–	0.011(5)	–	0.106(7)	–
Ti	0.88(16)	0.026(5)	–	0.85(8)	0.024(4)	–	0.43(5)	–	0.21(5)	–	0.182(7)	–	0.183(7)	–
Ga	13(8)	0.7(2)	–	20(2)	–	–	2.7(12)	–	0.41(12)	–	0.18(5)	–	0.209(4)	–
$Rb \times 10^3$	6(4)	–	–	9(3)	–	–	5.5(21)	–	0.43(10)	–	0.53(12)	–	2.0(6)	–
Sr	0.082(10)	–	–	0.070(8)	–	–	0.079(8)	–	0.127(13)	–	0.206(10)	–	0.195(9)	–
Y	1.1(3)	0.0057(18)	–	1.06(16)	–	–	0.51(5)	–	0.23(2)	–	0.178(9)	–	0.189(4)	–
Zr	0.8(3)	0.0031(20)	–	1.4(7)	0.0006(3)	–	0.15(3)	–	0.06(2)	–	0.0240(11)	–	0.028(4)	–
Nb	0.016(7)	–	–	0.013(5)	–	–	0.017(11)	–	0.020(13)	–	0.0037(7)	–	0.0047(13)	–
$Cs \times 10^4$	0.96(11)	–	–	53(11)	–	–	18(8)	–	1.0(6)	–	2.4(18)	–	1.4(4)	–
$Ba \times 10^4$	2.0(7)	–	–	51(7)	–	–	63(19)	–	7(3)	–	17.2(12)	–	28(4)	–
La	0.051(9)	–	–	0.066(6)	–	–	0.041(7)	–	0.059(11)	–	0.046(6)	–	0.055(3)	–
Nd	0.23(4)	–	–	0.39(18)	–	–	0.16(2)	–	0.16(3)	–	0.116(5)	–	0.131(4)	–
Sm	0.36(7)	0.00040(9)	–	0.43(6)	–	–	0.26(4)	–	0.21(3)	–	0.14(3)	–	0.172(5)	–
Yb	1.0(4)	0.030(16)	–	1.3(3)	0.050(12)	–	0.59(8)	–	0.22(3)	–	0.176(9)	–	0.187(7)	–
Pb	0.7(5)	0.41(4)	–	1.6(4)	0.69(18)	–	0.48(7)	–	0.8(4)	–	0.4(3)	–	0.17(6)	–

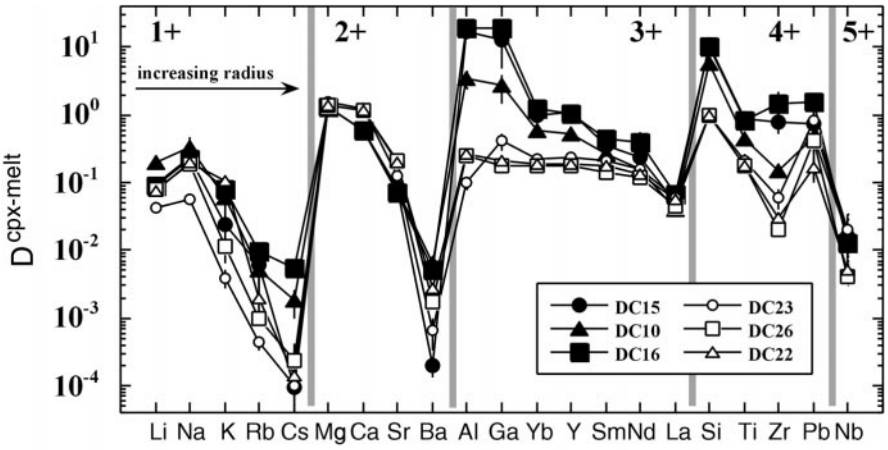

Fig. 4 Cpx-melt partition coefficients for silicate (Di-Ab) runs (*open symbols*) and carbonate (Di-Ab-Dmt) runs (*filled symbols*). Elements are ordered along the abscissa according to first ionic charge (increasing to right) and then ionic radius (also increasing to right). Comparison of silicate and carbonate melts shows marked differences for some elements, notably Ga, Al, Si, Zr, Ti, heavy REE, but overall similarity for others. Differences in partition coefficients between DC23 (0.8 GPa) and DC22/26 (3 GPa), especially for alkali metals and Al, reflect pressure differences. DC10 has elevated melt SiO_2 (9 wt%), and lower cpx CaTs (6 mol%) content relative to DC15/16 (5 wt% and 17 mol% respectively), and consequently partition coefficients tend towards those of the silicate melt runs (56 wt% SiO_2, 1 mol% CaTs). The irregular behaviour of Cs is an unavoidable result of glass contamination of crystal analyses (see text)

sensitive to CaTs than D_{Yb}, while $D_{cpx\text{-}sil}/D_{cpx\text{-}carb}$ shows the opposite trend from light to heavy REE (Fig. 5b). Moreover, variations in D_{Si} and D_{Al} with CaTs content are modest compared to the differences seen between Di-Ab and Di-Ab-Dmt runs. We consider this to be strong evidence that not all of the difference between Di-Ab and Di-Ab-Dmt runs can be ascribed to CaTs alone.

Several authors (e.g. Green et al. 1992; Klemme et al. 1995) have proposed that cpx-silicate melt and cpx-carbonate melt partitioning are strongly influenced by melt chemistry in the same way that trace elements are fractionated between coexisting silicate and carbonate liquids (Hamilton et al. 1989; Fielding 1992; Veksler et al. 1998). However, in none of the cpx-melt partitioning studies were the authors able to *directly* compare partition coefficients from carbonate and silicate systems under matched *P-T* conditions, and they could not rule out the possibility that *P-T* effects alone were the cause of the differences. This is especially problematic because, in general, cpx coexists with melt at lower temperature in carbonate-bearing systems than in carbonate-free systems. Figure 5a goes a long way to isolating the effects of melt composition from those of *P* and *T*, and so permits direct comparison with available partitioning data for immiscible silicate-carbonate melts. Unfortunately there are no experimental two-liquid partitioning data at 1375 °C or 3 GPa. However, two recent experimental studies at lower pressures and temperatures (0.5–1.5 GPa, 1200–1300 °C – Fielding 1992; 0.08–0.09 GPa, 965–1015 °C – Veksler et al. 1998) present partition coefficients ($D_{carb\text{-}sil}$) for many of the elements studied here. In Fig. 5c, we compare their $D_{carb\text{-}sil}$ values with our $D_{cpx\text{-}sil}/D_{cpx\text{-}carb}$ values. The agreement in both magnitude and pattern is striking, especially for the REE, Si, Al and Zr. The only significant mismatch occurs for the large alkali metals (Rb, Cs), suggesting that this may be a result of the large pressure difference between our experiments and the two-liquid experiments. Overall, the close agreement suggests that the primary control on the *different* partitioning behaviour of cpx in silicate melt and carbonate melt systems is melt structure rather than crystal chemistry. However, until the effect of CaTs on cpx-melt partitioning has been fully quantified by carefully designed experiments in simple systems (e.g. Hill et al. 2000), we cannot completely eliminate this important effect. Certainly we recognise that changing activity of the CaTs molecule in crystal *and* melt may produce complementary effects. Whatever the cause of the differences between Di-Ab and Di-Ab-Dmt systems, it is clear that the common practice of estimating cpx-carbonate melt partition coefficients from cpx-silicate melt partition coefficients by dividing the silicate melt values by $D_{carb\text{-}sil}$ is a good approximation, provided that *P-T* conditions are suitably matched.

Lattice strain

The dominant control on mineral-melt trace element partitioning is the ability of the relatively rigid crystal lattice to accommodate misfit cations, i.e. those of different size and/or charge to the host cation normally resident on a particular lattice site. This fact, first recognised by Goldschmidt (1937), is well illustrated by plots of partition coefficient versus ionic radius, so-called Onuma diagrams (Onuma et al. 1968). For a given series of isovalent cations entering a given lattice site, partition coefficients vary approximately parabolically with ionic radius. The maximum of the parabola reflects the optimum size of the lattice site, while the curvature of the parabola reflects the host crystal's ability to accommodate misfit cations (Blundy and Wood 1994). Where more than one site is available for substitution (e.g. T, M1 and M2 sites in cpx) a series of

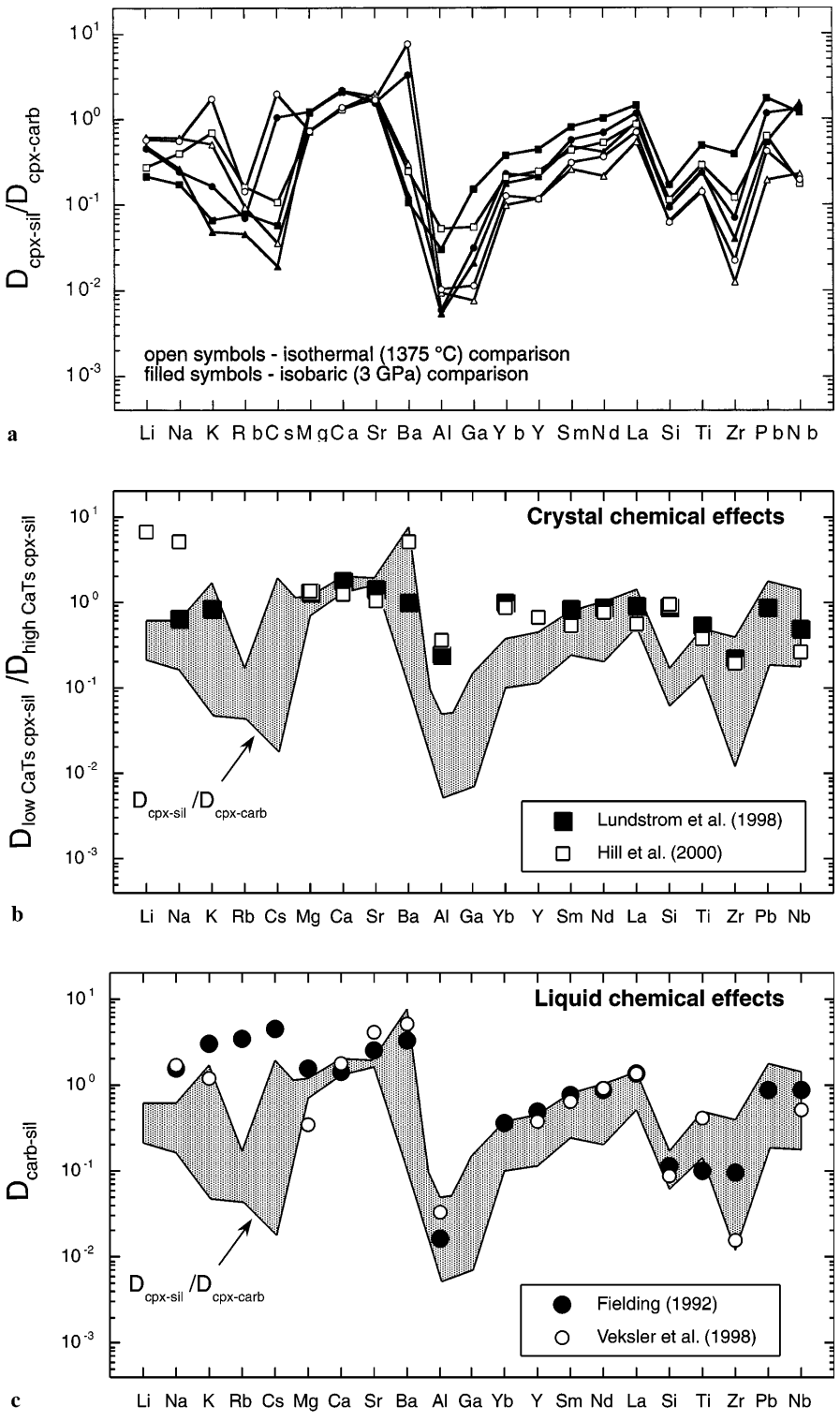

Fig. 5.a Ratio of cpx-silicate melt to cpx-carbonate melt partition coefficients ($D_{cpx-sil}/D_{cpx-carb}$) under isothermal (*open symbols*) and isobaric (*filled symbols*) conditions Elements ordered as in Fig. 4. $D_{cpx-sil}/D_{cpx-carb}$ was determined by dividing each cpx-carbonate melt partition coefficient into the partition coefficients from DC23 (isothermal comparison), or the average of DC22 and DC26 (isobaric comparison). Data for DC10 (*squares*), DC15 (*circles*) and DC16 (*triangles*) are shown as separate thin lines. Compared in this way *P-T* effects on partitioning are minimised. **b** Comparison of $D_{cpx-sil}/D_{cpx-carb}$ from **a** (*shaded field*) with the ratio of low CaTs to high CaTs cpx partition coefficients ($D_{low\ CaTs\ cpx-sil}/D_{high\ CaTs\ cpx-sil}$) from the isothermal experiments of Lundstrom et al. (1998) and Hill et al. (2000). $D_{low\ CaTs\ cpx-sil}/D_{high\ CaTs\ cpx-sil}$ shows some similarity to $D_{cpx-sil}/D_{cpx-carb}$ but in detail does not reproduce either the magnitude or the pattern of observed fractionations, especially for the REE. This suggests that, although crystal chemical effects are important, they are not the dominant control on $D_{cpx-sil}/D_{cpx-carb}$. **c** Comparison of $D_{cpx-sil}/D_{cpx-carb}$ (*shaded field*) with the experimental two-liquid partition coefficients ($D_{carb-sil}$) of Fielding (1992) and Veksler et al. (1998). Note that $D_{cpx-sil}/D_{cpx-carb}$ is quantitatively very similar to $D_{carb-sil}$ and faithfully reproduces the observed REE pattern and low values for Al, Si and Zr. Differences for large alkali metals may be a consequence of the significant pressure differences between the two data sets. The close similarity suggests an important role for melt chemistry in controlling $D_{cpx-sil}/D_{cpx-carb}$

overlapping parabolas are observed (e.g. Onuma et al. 1968; Purton et al. 1996).

In Fig. 6, we plot cpx-melt Onuma diagrams for one Di-Ab and two Di-Ab-Dmt experiments. Only large cations entering the M2-site are plotted. (An Onuma diagram for DC23 appears in Fig. 4a of Wood and Blundy 1997.) Overall, cpx from both Di-Ab and Di-Ab-Dmt runs show similar partitioning parabolas with maxima at approximately 1 Å, demonstrating the overarching importance of crystal structure. There are, however, subtle differences between parabolas for the Di-Ab and Di-Ab-Dmt systems, as discussed above. These are best illustrated by reference to the lattice strain model of Blundy and Wood (1994), which enables

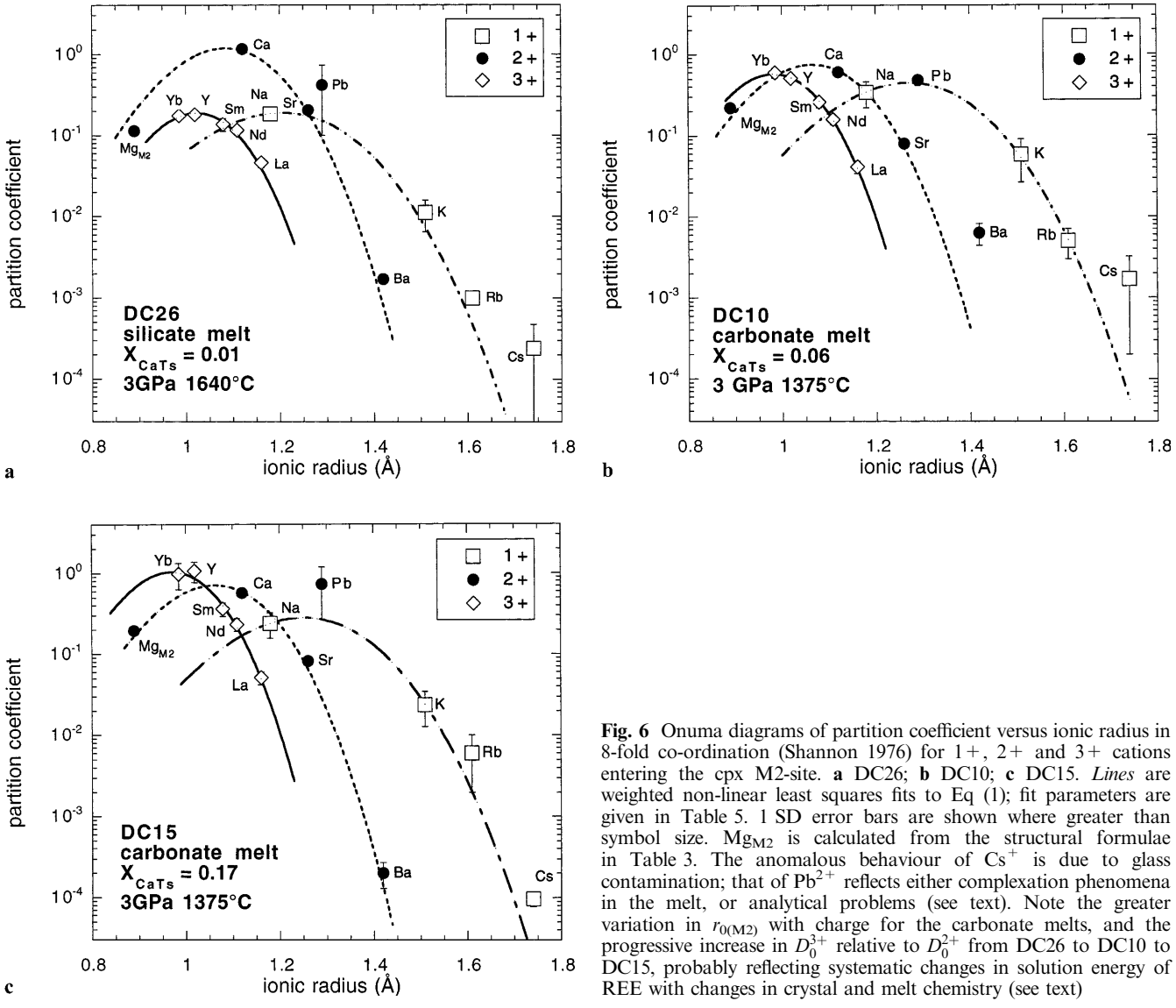

Fig. 6 Onuma diagrams of partition coefficient versus ionic radius in 8-fold co-ordination (Shannon 1976) for 1+, 2+ and 3+ cations entering the cpx M2-site. **a** DC26; **b** DC10; **c** DC15. *Lines* are weighted non-linear least squares fits to Eq (1); fit parameters are given in Table 5. 1 SD error bars are shown where greater than symbol size. Mg_{M2} is calculated from the structural formulae in Table 3. The anomalous behaviour of Cs^{+} is due to glass contamination; that of Pb^{2+} reflects either complexation phenomena in the melt, or analytical problems (see text). Note the greater variation in $r_{0(M2)}$ with charge for the carbonate melts, and the progressive increase in D_0^{3+} relative to D_0^{2+} from DC26 to DC10 to DC15, probably reflecting systematic changes in solution energy of REE with changes in crystal and melt chemistry (see text)

the parabolic variation in Onuma diagrams to be quantified and related to crystal chemical and physical parameters. The model describes partitioning of elements i with valence $n+$ entering lattice site α, in terms of r_i, the radius of i^{n+}, $r_{0(\alpha)}^{n+}$, the ideal site radius, E_α^{n+}, the effective Young's modulus of the site, and $D_{0(\alpha)}^{n+}$, the strain-free partition coefficient for a cation of radius $r_{0(\alpha)}^{n+}$:

$$D_{i^{n+}} = D_{0(\alpha)}^{n+} \times \exp\left\{\frac{-4\pi E_\alpha^{n+} N_A \left[\frac{r_{0(\alpha)}^{n+}}{2}(r_i - r_{0(\alpha)}^{n+})^2 + \frac{1}{3}(r_i - r_{0(\alpha)}^{n+})^3\right]}{RT}\right\} \quad (1)$$

where R is the gas constant, N_A is Avogadro's number and T is the temperature in K. $r_{0(\alpha)}$, E_α and $D_{0\alpha}$ are different for each valence group: E_α increases with increasing charge on the substituent ion (Blundy and Wood 1994; Wood and Blundy 1997), $D_{0(\alpha)}$ is typically lower for heterovalent than homovalent substitution (Blundy and Wood 1994), and $r_{0(\alpha)}$ tends to increase with decreasing charge (Van Westrenen et al. 1998; Law et al. 2000).

We have fitted Eq. (1) to all of the experiments reported here, in addition to the experimental data of Klemme et al. (1995) and Green et al. (1992) which also include a large number of trace elements. [Note that cpx-carbonate melt partition coefficients of Sweeney et al. (1995) are so consistently close to unity for a wide range of elements that we suspect some contamination of crystals by melt during PIXE analysis may have affected the results.] Fit parameters for Eq. (1) are highly correlated (Wood and Blundy 1997). A preliminary fit of our data revealed that E_{M2}^{3+} is consistently within error (±30 GPa) of values predicted by Eq. (14) of Wood and Blundy. Fitted E_{M2}^{1+} and E_{M2}^{2+} are approximately one third and two thirds respectively of E_{M2}^{3+}, in accordance with the observed dependence of E_α on cation charge (Blundy and Wood 1994; Wood and Blundy 1997). Therefore, in order to reduce cross-correlation in our fit parameters,

Table 5 Lattice strain parameters for cpx M2-site from fits of partitioning data to Eq (1). Run numbers in italic are from carbonate melt experiments; others from silicate melt. Uncertainties are 1 SD expressed in terms of last significant digits. nd. fit not determined, data too scattered

		DC15	DC10	DC16	DC23	DC26	DC22	K2[a]	K4[a]	GAS[b]
1+	E_{M2} (GPa)[c]	93	93	93	88	90	90	–	–	–
	r_0 (Å)	1.251(5)	1.270(16)	1.304(12)	1.234(8)	1.205(1)	nd	–	–	–
	D_0	0.28(1)	0.44(13)	0.36(7)	0.063(6)	0.19(1)	nd	–	–	–
2+	E_{M2} (GPa)[c]	187	187	187	177	180	181	189	189	–
	r_0 (Å)	1.063(4)	1.065(5)	1.061(5)	1.081(3)	1.085(1)	1.085(2)	1.088(20)	1.082(23)	–
	D_0	0.71(3)	0.74(4)	0.73(3)	1.32(3)	1.19(1)	1.15(2)	0.75(9)	0.69(9)	–
3+	E_{M2} (GPa)[c]	280	280	280	265	270	271	283	283	290
	r_0 (Å)	0.971(11)	0.983(6)	0.975(6)	1.030(7)	1.023(3)	1.028(4)	1.009(8)	nd	0.989(14)
	D_0	1.03(25)	0.57(5)	1.17(17)	0.243(14)	0.188(6)	0.202(5)	0.40(4)	nd	0.25(2)
	W&B[d] r_0 (Å)	1.022	1.025	1.022	1.033	1.031	1.031	1.024	1.029	–[e]

[a] Data from Klemme et al. (1995)
[b] Data from Green et al. (1992)
[c] Young's moduli for M2-site calculated from Eq. (2a–c) at the experimental P and T
[d] Calculated value of $r^{3+}_{0(M2)}$ from Wood and Blundy (1997)
[e] Major element mineral chemistry not reported by Green et al. (1992)

we imposed E_{M2} values for each charge, according to the following equations, and fitted for $D^{n+}_{0(M2)}$ and $r^{3+}_{0(M2)}$ only:

$$E^{1+}_{M2} = 106.2 + 2.3\,P - 0.012T \quad (2a)$$

$$E^{2+}_{M2} = 212.4 + 4.6\,P - 0.024T \quad (2b)$$

$$E^{3+}_{M2} = 318.6 + 6.9P - 0.036T \quad (2c)$$

E and P are in GPa, T is in K. Fit parameters are listed in Table 5, where model $r^{3+}_{0(M2)}$ values obtained by Wood and Blundy (1997) from REE partitioning data in anhydrous silicate melts are shown for comparison.

Several interesting features emerge from Table 5. First $r_{0(M2)}$ decreases with charge for both Di-Ab and Di-Ab-Dmt runs, as observed in garnet-melt (Van Westrenen et al. 1998) and wollastonite-melt (Law et al. 2000) partitioning studies, but not previously recognised for cpx. Note that $r^{3+}_{0(M2)}$ from Di-Ab runs is in excellent agreement with the values of Wood and Blundy (1997). Significantly, the rate of decrease in $r_{0(M2)}$ with charge is greater for carbonate melt than for silicate melt experiments, with a cross-over around 2+ (Fig. 7). This is the first reported experimental evidence that $r_{0(M2)}$, hitherto considered to be an exclusively crystal-controlled parameter (Blundy and Wood 1994; Wood and Blundy 1997), is influenced by melt composition.

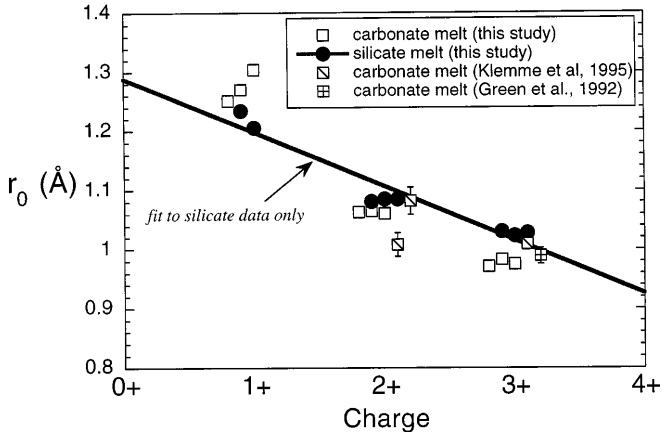

Fig. 7 Variation in $r_{0(M2)}$ with charge in silicate and carbonate systems. Data are from Table 5, with 1 SD error bars. Points are offset slightly along the abscissa to facilitate comparison. For silicate melts (*solid symbols*), $r_{0(M2)}$ decreases with ionic charge, as observed for other minerals. This variation is illustrated qualitatively by the *solid line*. For carbonate melts, including data of Green et al. (1992) and Klemme et al. (1995), a more extreme decrease is observed. This is ascribed to differences in complexation energy for cations in carbonate melt versus silicate melts (see text)

A second feature of note in Table 5 and Fig. 6 is the systematic difference in $D_{0(M2)}$ values for 1+, 2+ and 3+ cations between Di-Ab and Di-Ab-Dmt experiments. Thus in Di-Ab runs $D^{2+}_{0(M2)} \gg D^{3+}_{0(M2)} \approx D^{3+}_{0(M2)}$, as previously observed in other cpx-silicate melt runs (e.g. Blundy and Wood 1994). In contrast Di-Ab-Dmt runs show elevated $D^{3+}_{0(M2)}$ that may equal or exceed $D^{2+}_{0(M2)}$. In DC10 $D^{2+}_{0(M2)} \approx D^{3+}_{0(M2)} \approx D^{1+}_{0(M2)}$, while in DC15 and DC16, $D^{3+}_{0(M2)} > D^{2+}_{0(M2)} > D^{1+}_{0(M2)}$ (Fig. 6, Table 5). Evidently melt structure may also change the optimum cation charge at a given lattice site. In the following section we discuss these observations in terms of the energetics of trace element exchange between minerals and melts.

Energetics

Trace element partitioning between crystals and melts involves two, near-simultaneous substitutions: removal of the host cation from the crystal lattice site of interest and insertion of a trace cation; and removal of the trace cation from the melt and insertion of the host cation. In the case of M^{2+} exchanging for Ca^{2+} on the diopside M2-site, we can write

$$Ca^{2+}_{M2} \leftrightarrow M^{2+}_{M2} \quad (3a)$$

$$M^{2+}_{melt} \leftrightarrow Ca^{2+}_{melt} \quad (3b)$$

Both Eq. (3a) and (3b) can be considered as defect reactions with an associated finite defect energy. It is useful to consider this defect energy as consisting of two parts (e.g. Purton et al. 1996): an *initial defect energy* due to breaking one set of cation-anion bonds and forming another; and a *relaxation energy* due to readjustment of the positions of surrounding ions to accommodate the new cation. The sum of the initial defect energy and relaxation energy is termed the *final defect energy*. The magnitude of the initial defect energy depends on the nature of the co-ordinating anion (O^{2-}, F^{-}, CO_3^{2-} etc), and the co-ordination number, while the relaxation energy is related to the structure of the host material (crystal or melt), and its elastic properties. To a first approximation the initial defect energy will be similar in crystal and melt, provided that the co-ordinating anions and co-ordination number of M^{2+} and Ca^{2+} are the same in both phases. This effective cancellation of initial defect energies will result in a solution energy for the exchange reaction, i.e. Eq. (3a) + (3b)

$$Ca^{2+}_{M2} + M^{2+}_{melt} = M^{2+}_{M2} + Ca^{2+}_{melt} \quad (3c)$$

that is controlled by the difference in relaxation energies between crystal and melt. Because crystal structures are typically more rigid than melt structures, the solution energy will tend to be dominated by the relaxation energy of the crystal. This is the explicit assumption at the heart of the lattice strain model (e.g. Brice 1975; Blundy and Wood 1994). It is borne out by lattice statics computer simulations of partitioning (e.g. Purton et al. 1996; Van Westrenen et al. 2000b), which demonstrate that the crystal relaxation energy varies parabolically with ionic radius in a fashion that closely resembles variations in mineral-melt partition coefficients (e.g. Fig. 6). The calculated relaxation energies can be fit to the Brice model [Eq. (1)] to yield values for $r_{0(\alpha)}$ and E_α that are similar to those observed in experimental studies of the same crystal phase.

In reality, although the relaxation energy of the melt is less than that of the crystal, it is not necessarily negligible, and may make a significant contribution to the overall solution energy. The form of relaxation energy versus ionic radius relationship in the melt is not known, and cannot be directly calculated using lattice statics techniques. It is important, however, to note that, whatever form it takes, the melt relaxation energy should be added to the crystal relaxation energy to obtain a closer approximation to the solution energy. For example, if the melt relaxation energy varies linearly with ionic radius, the effect of adding the melt and crystal relaxation energies will be to produce a second parabola, broadly similar to the crystal relaxation energy parabola, but displaced in terms of its $r_{0(\alpha)}$ and E_α. To illustrate this, in Fig. 8 we show the effects of adding a crystal relaxation energy parabola centred about the M2 site in diopside ($r_{0(M2)} = r_{Ca} = 1.12$ Å; $E_{M2} = 200$ GPa), to a hypothetical melt relaxation energy that increases linearly with ionic radius (80 kJ mol^{-1} Å^{-1}). Note that the resultant is also a parabola, which can be described by Eq. (1), but that $r_{0(M2)}$ has shifted to less than 1.12 Å, and

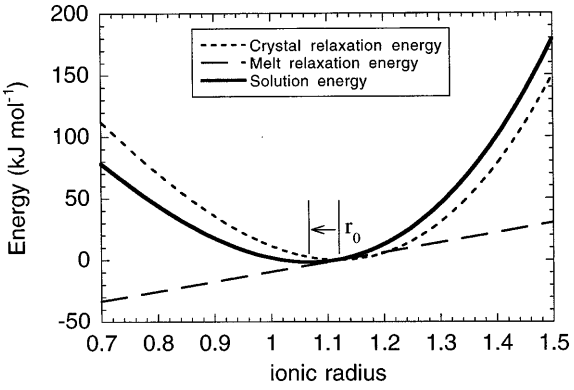

Fig. 8 Illustration of the likely effect of melt structure on the parameters $r_{0(\alpha)}$ and E_α, due to the non-zero relaxation energy of silicate melts. The *thin dotted curve* denotes the relaxation energy around an 8-fold co-ordinated crystal site occupied by Ca^{2+} ($r_0 = 1.12$ Å), with Young's modulus $E_\alpha = 200$ GPa, calculated using Eq. (1). The *thin broken line* denotes the (hypothetical) linear variation in relaxation energy around an eight-fold co-ordinated Ca^{2+} site in the co-existing melt. The *solid bold line* is the resultant obtained by adding the crystal and melt relaxation energies. This curve can also be fit to Eq. (1), with parameters $r_{0(M2)}$ (1.068 Å) and E_{M2} (189 GPa) that are significantly different from the crystal relaxation energy parameters. Note that in this example the overall variation in melt relaxation energy is small (~60 kJ mol^{-1}) compared to that for the crystal (~150 kJ mol^{-1})

$E_{M2} < 200$ GPa. The magnitude of the shift in $r_{0(\alpha)}$ and E_α is a function of the slope of the melt relaxation energy-ionic radius trend: a flatter trend would give a smaller shift, and vice versa. Likely causes of changes in the form of the melt relaxation energy-ionic radius trend are changes in the co-ordination environment of cations in the melt (e.g. from six- to four-fold), or changes in the co-ordinating anion (e.g. from O^{2-} to CO_3^{2-}).

From the previous discussion and Fig. 8 it is readily apparent how changes in melt chemistry and structure may influence $r_{0(\alpha)}$ and E_α. Unfortunately, there are no experimental or simulation data pertaining to the variation in defect energies of cations in silicate melts with which to test the predictions of Fig. 8. An alternative approach, employed in lattice statics simulations, is to approximate the final defect energy of reaction (3b) using the lattice energy differences (ΔU_{latt}) between isostructural phases of suitable composition, e.g. MO and CaO or MCO_3 and $CaCO_3$, to simulate the melt phase. ΔU_{latt} is then added to the calculated final defect energy of reaction (3a) to produce an estimate of the *solution energy* [reaction (3c)] at 0 K. Previous studies (Purton et al. 1996; Van Westrenen et al. 2000b) have found that variations in solution energy calculated in this way are, like the variations in crystal relaxation energy, parabolic with ionic radius and can be fitted to Eq. (1). Typically, the solution energy parabola has a different value of $r_{0(\alpha)}$ and E_α than the crystal relaxation energy parabola. More importantly, Van Westrenen et al. (2000b) noted that if different assumptions about the trace element melt "species" are made when calculating ΔU_{latt}, different fit values of $r_{0(\alpha)}$ and E_α for the solution energy parabola result. Thus, in modelling exchange equilibria of REE

between the pyrope X-site and silicate melt, Van Westrenen et al. (2000b) found that when REE_2O_3 is used as the melt species, fits of Eq. (1) to the solution energy give $r_{0(x)} = 0.85 \pm 0.01$ Å and $E_x = 550 \pm 40$ GPa, while when a YAG-type component is used ($REE_3Al_5O_{12}$) $r_{0(x)} = 0.73 \pm 0.03$ Å and $E_x = 210 \pm 20$ GPa. These findings were used by Van Westrenen et al. (2000b) to propose that melt structure may exert some influence on $r_{0(x)}$ and E_x and that these should not be considered as exclusively crystal-controlled parameters. Our experimental results corroborate this view, especially in the case of heterovalent substituents (Fig. 7), when the substitution of charge-balancing defects into crystal and melt must also be taken into account. Variation in $D^{n+}_{0(M2)}$ with charge, as described above, may also originate in this way as the ease of charge-balancing, for example by Al↔Si exchange, is likely to be very different in silicate versus carbonate melts.

We conclude that the observed differences between $r_{0(\alpha)}$ and E_α for silicate melt versus carbonate melt partitioning parabolas are consistent qualitatively with a change from O^{2-} to CO_3^{2-} as the principal co-ordinating (or complexing) anion for many trace cations in the melt. In other words, the parabolic variation in solution energy with ionic radius is characterised by different values of $r_{0(\alpha)}$ and E_α in the two simple end member exchange reactions that best describe silicate melt and carbonate melt partitioning, i.e.:

$$MO_{(sil\text{-}melt)} + Ca_{M2} = M_{M2} + CaO_{(sil\text{-}melt)} \quad (4a)$$

$$MCO_{3(carb\text{-}melt)} + Ca_{M2} = M_{M2} + CaCO_{3(carb\text{-}melt)} \quad (4b)$$

In this context it is worth noting that in their experimental study of garnet-hydrous melt partitioning (up to 20 wt% dissolved H_2O in the melt), Green et al. (2000) obtained very similar values of $r_{0(x)}$ and $E_{(x)}$ to those obtained by Van Westrenen et al. (1999, 2000a) under anhydrous conditions. Evidently the addition of water to melts has a much smaller effect on $r_{0(\alpha)}$ and E_α than the addition of CO_2. Even in the case of cpx partitioning with carbonate melts the effect is small (~0.04 Å, ~30 GPa) and by no means invalidates the parameterisation of $r_{0(M2)}$ and E_{M2} for cpx of Wood and Blundy (1997). We note also that where a cation shows distinct complexation behaviour in the melt relative to isovalent cations of similar size, marked deviations for the partitioning parabola may be expected. Law et al. (2000) have used similar arguments to account for anomalies in the partitioning of some 2+ cations between wollastonite and carbonate melt, and that explanation may account for the unusual behaviour of Pb^{2+} in the experiments reported here (Fig. 6). Further experiments on melts with high concentrations of other anion species, such as halides or phosphate, are required to test these proposals.

Application to carbonate melt metasomatism

A full discussion of carbonatite petrogenesis and mantle metasomatism is beyond the scope of this work. However, for the benefit of geochemists working on these and related problems, we can draw several potentially useful inferences. Firstly, the primary difference between cpx-silicate melt and cpx-carbonate melt partitioning derives from differences in melt structure. A reasonable approximation to cpx-carbonate melt partition coefficients can therefore be made by dividing cpx-silicate melt partition coefficients by $D_{carb\text{-}sil}$ provided that *P-T* and crystal composition are properly matched.

Secondly, the similarity of our experimental melt and cpx compositions to those obtained in experiments on the CMAS-CO_2 solidus, suggests that, although our primary aim was to elucidate the *systematics* of partitioning, our data has direct relevance to partial melting of carbonated lherzolite at ~3 GPa. This claim is strengthened by the fact that the only component of significance lacking from the CMAS-CO_2 system, when considering carbonate melt generation in the mantle, is FeO. As primary carbonatites are characterised by elevated *mg*-numbers in the range 0.80–0.90 (e.g. Sweeney 1994), the lack of this component has little bearing on phase relations. From the point of view of partitioning, Wood and Blundy (1997) have shown that variations in *mg*-number have a directly proportional effect on REE partitioning. Thus for small differences in *mg*-number between CMAS-CO_2 and nature, i.e.1.0 to 0.8, the effect on partition coefficients is negligible (±20% relative).

Thirdly, partitioning behaviour appears to change systematically with melt silica content (Fig. 4). We do not yet have enough data to discern whether this variation is linear. Suffice to say that for practical purposes experiments DC15 and DC10 (Table 4) bracket the likely range of cpx-melt partition coefficients during melting of carbonated lherzolite up to the point of exhaustion of a residual carbonate phase. Further experiments are required to fully characterise the change in partitioning as liquids evolve smoothly from carbonate at the solidus to silicate with increased degree of melting (Dalton and Presnall 1998b; Moore and Wood 1998).

Finally, our results can be used to shed some light on the different chemical styles of silicate melt versus carbonate melt metasomatism of mantle rocks. The elevated partition coefficients for Zr, Ti, Al, Ga and HREE in carbonate systems relative to silicate systems (Fig. 5a) means that during low degree melting of carbonated lherzolite these elements will be preferentially retained in the cpx-bearing residue. Melts will be characterised by overall highly elevated incompatible trace element concentrations (due to low degree of melting) with marked depletions of Al, Ga, Zr and Ti (but not necessarily Nb) and steep REE patterns. In fact these are widespread and diagnostic feature of carbonatites (Nelson et al. 1988; Woolley and Kempe 1989). As these melts migrate through, and react with, carbonate-free lherzolites at shallower depths they will undergo a variety of dissolution–precipitation reactions principally involving cpx (e.g. Dalton and Wood 1993). Cpx precipitated directly from carbonate melt will show overall elevated incompatible elements with negative anomalies for Al, Ga, Ti,

Zr and HREE. Hauri et al. (1993) describe cpx with precisely these characteristics in carbonate-metasomatised peridotites from the western Pacific. Cpx that forms as a result of progressive wall rock reaction will show a range of trace element signatures between incompatible element-depleted with modest HFSE anomalies, characteristic of lherzolites (Johnson et al. 1990), and incompatible element-rich with negative Zr and Ti anomalies, characteristic of carbonatites. Significantly, the contrast in trace element concentration and pattern between reactants (carbonate melt and lherzolite cpx) during this process makes it uniquely amenable to modelling by chromatography or reactive melt transport (e.g. Navon and Stolper 1987; Reiners 1998).

Acknowledgements J.B. would like to thank the Royal Society for a University Research Fellowship, and the Fulbright Commission for partial funding of sabbatical leave at the University of Oregon, Eugene, where this work was written up. J.D. acknowledges support of NSF grants EAR-9219159 and EAR-9725900 awarded to D.C. Presnall. We thank R.W. Hinton and J.A. Craven for their sterling efforts with the NSS ion-probe, R.A. Brooker for FTIR analyses, D.C. Presnall, K.M. Law, W. Van Westrenen and B.J. Wood for illuminating discussions, A.D. Johnston for hospitality in Eugene, and D. Batty for his careful distribution. R.J. Sweeney and G.M. Yaxley and W. Van Westrenen provided helpful and encouraging reviews.

References

Beattie P (1994) Systematics and energetics of trace-element partitioning between olivine and silicate melts: implications for the nature of mineral/melt partitioning. Chem Geol 117: 57–71

Beattie P, Ford C, Russell D (1991) Partition coefficients for olivine-melt and orthopyroxene-melt systems. Contrib Mineral Petrol 109: 212–224

Blundy JD, Wood BJ (1994) Prediction of crystal-melt partition coefficients from elastic moduli. Nature 372: 452–454

Blundy JD, Falloon TJ, Wood BJ, Dalton JA (1995) Sodium partitioning between clinopyroxene and silicate melts. J Geophys Res 100: 15501–15516

Blundy JD, Robinson JAC, Wood BJ (1998) Heavy REE are compatible in clinopyroxene on the spinel lherzolite solidus. Earth Planet Sci Lett 160: 493–504

Brenan JM, Watson EB (1991) Partitioning of trace elements between carbonate melt and clinopyroxene and olivine at mantle P-T conditions. Geochim Cosmochim Acta 55: 2203–2214

Brenan JM, Neroda E, Lundstrom CC, Shaw HF, Ryerson FJ, Phinney DL (1998) Behaviour of boron, beryllium and lithium during melting and crystallisation: constraints form mineral-melt partitioning experiments. Geochim Cosmochim Acta 62: 2129–2141

Brice JC (1975) Some thermodynamic aspects of the growth of strained crystals. J Crystal Growth 28: 249–253

Colson RO, McKay GA, Taylor LA (1988) Temperature and composition dependencies of trace element partitioning: olivine/melt and low-Ca pyroxene/melt. Geochim Cosmochim Acta 52: 539–553

Coltorti M, Bonadiman C, Hinton RW, Siena F, Upton BGJ (1998) Carbonatite metasomatism of the oceanic upper mantle: evidence from clinopyroxene and glasses in ultramafic xenoliths of Grand Comore, Indian Ocean. J Petrol 40: 133–165

Dalton JA, Lane SJ (1996) Electron microprobe analysis of Ca in olivine close to grain boundaries: the problem of secondary X-ray fluorescence. Am Mineral 81: 194–201

Dalton JA, Presnall DC (1998a) Carbonatitic melts along the solidus of model lherzolite in the system CaO-MgO-Al_2O_3-SiO_2-CO_2 from 3 to 7 GPa. Contrib Mineral Petrol 131: 123–135

Dalton JA, Presnall DC (1998b) The continuum of primary carbonatitic–kimberlitic melt compositions in equilibrium with lherzolite: data from the system CaO-MgO-Al_2O_3-SiO_2-CO_2 at 6 GPa. J Petrol 39: 1953–1964

Dalton JA, Wood BJ (1993) The compositions of primary carbonate melts and their evolution through wallrock reaction in the mantle. Earth Planet Sci Lett 119: 511–525

Dautria JM, Dupuy C, Takherist D, Dostal J (1992) Carbonate metasomatism in the lithospheric mantle: peridotitic xenoliths from a melilititic district of the Sahara basin. Contrib Mineral Petrol 111: 37–52

Ertel W, O'Neill HStC, Sylvester PJ, Dingwell DB (1999) Solubilities of Pt and Rh in a haplobasaltic silicate melt at 1300 °C. Geochim Cosmochim Acta 63: 2439–2449

Fielding KD (1992) Element partitioning between coexisting carbonate and silicate liquids. PhD Thesis, Univ Edinburgh

Gaetani GA, Grove TL (1995) Partitioning of rare earth elements between clinopyroxene and silicate melt: crystal-chemical controls. Geochim Cosmochim Acta 59: 1951–1962

Goldschmidt VM (1937) The principles of the distribution of chemical elements in minerals and rocks. J Chem Soc Lond 140: 655–673

Green DH, Wallace ME (1988) Mantle metasomatism by ephemeral carbonatite melts. Nature 336: 459–462

Green TH, Adam J, Sie SH (1992) Trace element partitioning between silicate minerals and carbonatite at 25 kbar and application to mantle metasomatism. Mineral Petrol 46: 179–184

Green TH, Blundy JD, Adam J, Yaxley GM (2000) SIMS determination of trace element partition coefficients between garnet, clinopyroxene and hydrous basaltic liquids at 2–7.5 GPa and 1080–1200 °C. Lithos (in press)

Hamilton DL, Bedson P, Esson J (1989) The behaviour of trace elements in the evolution of carbonatites. In: Bell K (ed) Carbonatites: genesis and evolution. Unwin Hyman, London, pp 405–427

Hauri EH, Shimizu N, Dieu JJ, Hart SR (1993) Evidence for hotspot-related carbonatite metasomatism in the oceanic upper mantle. Nature 365: 221–227

Hill E, Wood BJ, Blundy JD (2000) Effect of calcium-tschermaks component on trace element partitioning between clinopyroxene and silicate melt. Lithos (in press)

Hinton RW (1990) Ion microprobe trace-element analyses of silicates: measurement of multi-element glasses. Chem Geol 83: 11–25

Hunter RH, McKenzie D (1989) The equilibrium geometry of carbonate melts in rocks of mantle composition. Earth Planet Sci Lett 92: 347–356

Ionov DA, Dupuy C, O'Reilly SY, Koplova MG, Genshaft Y (1993) Carbonated peridotite xenoliths from Spitsbergen: implications for trace element signature of mantle carbonate metasomatism. Earth Planet Sci Lett 119: 283–297

Ionov DA, O'Reilly SY, Genshaft Y, Koplova MG (1996) Carbonate-bearing mantle peridotite xenoliths from Spitsbergen: phase relationships, mineral compositions and trace element residence. Contrib Mineral Petrol 125: 375–392

Irving AJ, Frey FA (1984) Trace element abundances in megacrysts and their host basalts: constraints on partition coefficients and megacryst genesis. Geochim Cosmochim Acta 48: 1201–1221

Johnson KTM, Dick HJB, Shimizu N (1990) Melting in the oceanic upper mantle: an ion microprobe study of diopsides in abyssal peridotites. J Geophys Res 95: 2661–2678

Klemme S, van der Laan SR, Foley SF, Günther D (1995) Experimentally determined trace and minor element partitioning between clinopyroxene and carbonatite melt under upper mantle conditions. Earth Planet Sci Lett 133: 439–448

Kogarko LN (1993) Geochemical characteristics of oceanic carbonatites from the Cape Verde Islands. S Afr J Geol 96: 119–125

Lane SJ, Dalton JA (1994) Electron microprobe analysis of geological carbonates. Am Mineral 79: 745–749

Law KM, Blundy JD, Wood BJ, Ragnarsdottir KV (1998) Partitioning of trace elements between calcite and silicate carbonate melt in the system $CaCO_3$-SiO_2-CO_2 at high temperatures and pressures. EOS Trans Am Geophys Union 79: F882

Law KM, Blundy JD, Wood BJ, Ragnarsdottir KV (2000) Trace element partitioning between wollastonite and silicate-carbonate melt. Mineral Mag (in press)

Lundstrom CC, Shaw HF, Ryerson FJ, Williams Q, Gill J (1998) Crystal chemical control of clinopyroxene-melt partitioning in the Di-Ab-An system: implications for elemental fractionations in the depleted mantle. Geochim Cosmochim Acta, 62: 2849–2862

McInnes BIA, Cameron EM (1994) Carbonated, alkaline hybridizing melts from a sub-arc environment: mantle wedge samples from the Tabar-Lihir-Tanga-Feni arc, Papua New Guinea. Earth Planet Sci Lett 122: 125–141

Moore KM, Wood BJ (1998) The transition from carbonate to silicate melts in the CaO-MgO-SiO_2-CO_2 system. J Petrol 39: 1943–1952

Navon O, Stolper EM (1987) Geochemical consequences of melt percolation: the upper mantle as a chromatographic column. J Geol 95: 285–307

Nelson DR, Chivas AR, Chappell BW, McCulloch MT (1988) Geochemical and isotopic systematics in carbonatites and implications for the evolution of ocean-island sources. Geochim Cosmochim Acta 52: 1–17

Onuma N, Higuchi H, Wakita H, Nagasawa H (1968) Trace element partition between two pyroxenes and the host lava. Earth Planet Sci Lett 5: 47–51

Purton JA, Allan NL, Blundy JD, Wasserman EA (1996) Isovalent trace element partitioning between minerals and melts – a computer simulation study. Geochim Cosmochim Acta 60: 4977–4987

Purton JA, Allan NL, Blundy JD (1997) Calculated solution energies of heterovalent cations in forsterite and diopside: implications for trace element partitioning. Geochim Cosmochim Acta 61: 3927–3936

Purton JA, Blundy JD, Allan NL (2000) Computer simulation of high temperature forsterite-melt partitioning. Am Mineral (in press)

Reiners PW (1998) Reactive melt transport in the mantle and geochemical signatures of mantle-derived magmas. J Petrol 39: 1039–1061

Rudnick RL, McDonough WF, Chappell BW (1993) Carbonatite metasomatism in the northern Tanzanian mantle: petrographic and geochemical characteristics. Earth Planet Sci Lett 114: 463–475

Salters VJM, Longhi J (1999) Trace element partitioning during the initial stages of melting beneath mid-ocean ridges. Earth Planet Sci Lett 166: 15–30

Schiano P, Clocchiatti R, Shimizu N, Weis D, Mattielli N (1994) Cogenetic silica-rich and carbonate-rich melts trapped in mantle minerals in Kerguelen ultramafic xenoliths: implications for metasomatism in the oceanic upper mantle. Earth Planet Sci Lett 123: 167–178

Shannon RD (1976) Revised effective ionic radii and systematic studies of interatomic distances in halides and chalcogenides. Acta Cryst A32: 751–767

Sweeney RJ (1994) Carbonatite melt compositions in the Earth's mantle. Earth Planet Sci Lett 128: 259–270

Sweeney RJ, Prozesky V, Przybylowicz W (1995) Selected trace and minor element partitioning between peridotite minerals and carbonatite melts at 18–46 kbar pressure. Geochim Cosmochim Acta 59: 3671–3683

Taura H, Yurimoto H, Kurita K, Sueno S (1998) Pressure dependence on partition coefficients for trace elements between olivine and the coexisting melts. Phys Chem Miner 25: 469–484

Van Westrenen W, Blundy JD, Purton JA, Wood BJ (1998) Towards a predictive model for garnet-melt trace element partitioning: experimental and computational results. Mineral Mag 62A: 1580–1581

Van Westrenen W, Blundy JD, Wood BJ (1999) Crystal-chemical controls on trace element partitioning between garnet and anhydrous silicate melt. Am Mineral 84: 838–847

Van Westrenen W, Blundy JD, Wood BJ (2000a) Effect of Fe^{2+} on garnet-melt trace element partitioning: experiments in FCMAS and quantification of crystal-chemical controls in natural systems. Lithos (in press)

Van Westrenen W, Allan NL, Blundy JD, Purton JA, Wood BJ (2000b) Static lattice energy computer simulations of trace element incorporation into garnets – comparison with experimental garnet-melt partitioning data. Geochim Cosmochim Acta (in press)

Veksler IV, Petibon C, Jenner GA, Dorfman AM, Dingwell DB (1998) Trace element partitioning in immiscible silicate-carbonate liquid systems: an initial experimental study using a centrifuge autoclave. J Petrol 39: 2095–2104

Wallace ME, Green DH (1988) An experimental determination of primary carbonatite composition. Nature 335: 343–346

Watson EB (1979) Calcium content of forsterite coexisting with silicate liquid in the system Na_2O-CaO-MgO-Al_2O_3-SiO_2. Am Mineral 64: 824–829

Wood BJ, Blundy JD (1997) A predictive model for rare earth element partitioning between clinopyroxene and anhydrous silicate melt. Contrib Mineral Petrol 129: 166–181

Woolley AR, Kempe DRC (1989) Carbonatites: nomenclature, average chemical compositions, and element distribution. In: Bell K (ed) Carbonatites: genesis and evolution. Unwin Hyman, London, pp 1–14

Wyllie PJ, Lee W-J (1998) Model system controls on conditions of formation of magnesiocarbonatite and calciocarbonatite magmas from the mantle. J Petrol 39: 1885–1894

Yaxley GM, Crawford AJ, Green DH (1991) Evidence for carbonatite metasomatism in spinel peridotite xenoliths from western Victoria, Australia. Earth Planet Sci Lett 107: 305–317

Yaxley GM, Green DH, Kamenetsky V (1998) Carbonatite metasomatism in the southeastern Australian lithosphere. J Petrol 39: 1917–1930